

# Measurement of Ratios of $\nu_\mu$ Charged-Current Cross Sections on C, Fe, and Pb to CH at Neutrino Energies 2–20 GeV

B.G. Tice,<sup>1,\*</sup> M. Datta,<sup>2</sup> J. Mousseau,<sup>3</sup> L. Aliaga,<sup>4,5</sup> O. Altinok,<sup>6</sup> M.G. Barrios Sazo,<sup>7</sup> M. Betancourt,<sup>8</sup> A. Bodek,<sup>9</sup> A. Bravar,<sup>10</sup> W.K. Brooks,<sup>11</sup> H. Budd,<sup>9</sup> M. J. Bustamante,<sup>5</sup> A. Butkevich,<sup>12</sup> D.A. Martinez Caicedo,<sup>13,8</sup> C.M. Castromonte,<sup>13</sup> M.E. Christy,<sup>2</sup> J. Chvojka,<sup>9</sup> H. da Motta,<sup>13</sup> J. Devan,<sup>4</sup> S.A. Dytman,<sup>14</sup> G.A. Díaz,<sup>5</sup> B. Eberly,<sup>14</sup> J. Felix,<sup>7</sup> L. Fields,<sup>15</sup> G.A. Fiorentini,<sup>13</sup> A.M. Gago,<sup>5</sup> H. Gallagher,<sup>6</sup> R. Gran,<sup>16</sup> D.A. Harris,<sup>8</sup> A. Higuera,<sup>7</sup> K. Hurtado,<sup>13,17</sup> M. Jerkins,<sup>18</sup> T. Kafka,<sup>6</sup> M. Kordosky,<sup>4</sup> S.A. Kulagin,<sup>12</sup> T. Le,<sup>1</sup> G. Maggi,<sup>11,†</sup> E. Maher,<sup>19</sup> S. Manly,<sup>9</sup> W.A. Mann,<sup>6</sup> C.M. Marshall,<sup>9</sup> C. Martin Mari,<sup>10</sup> K.S. McFarland,<sup>9,8</sup> C.L. McGivern,<sup>14</sup> A.M. McGowan,<sup>9</sup> J. Miller,<sup>11</sup> A. Mislivec,<sup>9</sup> J.G. Morfin,<sup>8</sup> T. Muhlbeier,<sup>13</sup> D. Naples,<sup>14</sup> J.K. Nelson,<sup>4</sup> A. Norrick,<sup>4</sup> J. Osta,<sup>8</sup> J.L. Palomino,<sup>13</sup> V. Paolone,<sup>14</sup> J. Park,<sup>9</sup> C.E. Patrick,<sup>15</sup> G.N. Perdue,<sup>8,9</sup> L. Rakotondravohitra,<sup>8,‡</sup> R.D. Ransome,<sup>1</sup> H. Ray,<sup>3</sup> L. Ren,<sup>14</sup> P.A. Rodrigues,<sup>9</sup> D. G. Savage,<sup>8</sup> H. Schellman,<sup>15</sup> D.W. Schmitz,<sup>20</sup> C. Simon,<sup>21</sup> F.D. Snider,<sup>8</sup> C.J. Solano Salinas,<sup>17</sup> N. Tagg,<sup>22</sup> E. Valencia,<sup>7</sup> J.P. Velásquez,<sup>5</sup> T. Walton,<sup>2</sup> J. Wolcott,<sup>9</sup> G. Zavala,<sup>7</sup> D. Zhang,<sup>4</sup> and B.P. Ziemer<sup>21</sup>

(MINERvA Collaboration)

<sup>1</sup>*Rutgers, The State University of New Jersey, Piscataway, New Jersey 08854, USA*

<sup>2</sup>*Hampton University, Dept. of Physics, Hampton, VA 23668, USA*

<sup>3</sup>*University of Florida, Department of Physics, Gainesville, FL 32611*

<sup>4</sup>*Department of Physics, College of William & Mary, Williamsburg, Virginia 23187, USA*

<sup>5</sup>*Sección Física, Departamento de Ciencias, Pontificia Universidad Católica del Perú, Apartado 1761, Lima, Perú*

<sup>6</sup>*Physics Department, Tufts University, Medford, Massachusetts 02155, USA*

<sup>7</sup>*Campus León y Campus Guanajuato, Universidad de Guanajuato, Lascruain*

*de Retana No. 5, Col. Centro. Guanajuato 36000, Guanajuato México.*

<sup>8</sup>*Fermi National Accelerator Laboratory, Batavia, Illinois 60510, USA*

<sup>9</sup>*University of Rochester, Rochester, New York 14610 USA*

<sup>10</sup>*University of Geneva, Geneva, Switzerland*

<sup>11</sup>*Departamento de Física, Universidad Técnica Federico Santa María, Avda. España 1680 Casilla 110-V, Valparaíso, Chile*

<sup>12</sup>*Institute for Nuclear Research of the Russian Academy of Sciences, 117312 Moscow, Russia*

<sup>13</sup>*Centro Brasileiro de Pesquisas Físicas, Rua Dr. Xavier Sigaud 150, Urca, Rio de Janeiro, RJ, 22290-180, Brazil*

<sup>14</sup>*Department of Physics and Astronomy, University of Pittsburgh, Pittsburgh, Pennsylvania 15260, USA*

<sup>15</sup>*Northwestern University, Evanston, Illinois 60208*

<sup>16</sup>*Department of Physics, University of Minnesota – Duluth, Duluth, Minnesota 55812, USA*

<sup>17</sup>*Universidad Nacional de Ingeniería, Apartado 31139, Lima, Perú*

<sup>18</sup>*Department of Physics, University of Texas, 1 University Station, Austin, Texas 78712, USA*

<sup>19</sup>*Massachusetts College of Liberal Arts, 375 Church Street, North Adams, MA 01247*

<sup>20</sup>*Enrico Fermi Institute, University of Chicago, Chicago, IL 60637 USA*

<sup>21</sup>*Department of Physics and Astronomy, University of California, Irvine, Irvine, California 92697-4575, USA*

<sup>22</sup>*Department of Physics, Otterbein University, 1 South Grove Street, Westerville, OH, 43081 USA*

(Dated: March 11, 2015)

We present measurements of  $\nu_\mu$  charged-current cross section ratios on carbon, iron, and lead relative to a scintillator (CH) using the fine-grained MINERvA detector exposed to the NuMI neutrino beam at Fermilab. The measurements utilize events of energies  $2 < E_\nu < 20$  GeV, with  $\langle E_\nu \rangle = 8$  GeV, which have a reconstructed  $\mu^-$  scattering angle less than  $17^\circ$  to extract ratios of inclusive total cross sections as a function of neutrino energy  $E_\nu$  and flux-integrated differential cross sections with respect to the Bjorken scaling variable  $x$ . These results provide the first high-statistics direct measurements of nuclear effects in neutrino scattering using different targets in the same neutrino beam. Measured cross section ratios exhibit a relative depletion at low  $x$  and enhancement at large  $x$ . Both become more pronounced as the nucleon number of the target nucleus increases. The data are not reproduced by GENIE, a conventional neutrino-nucleus scattering simulation, or by the alternative models for the nuclear dependence of inelastic scattering that are considered.

PACS numbers: 13.15.+g, 25.30.Pt, 21.10.-k

Measurements of charged lepton scattering from different nuclei show that the cross section ratio on a heavy nucleus relative to the deuteron  $\sigma^A/\sigma^D$  deviates from

unity by as much as 20%. This demonstrates nontrivial nuclear effects over a wide range of Bjorken's scaling variable  $x$  [1–4]. These observations, first reported

by the European Muon Collaboration (EMC) [5, 6] in 1983, signal a difference in the quark-parton structure of bound nucleons from that of free nucleons and have triggered theoretical exploration of background nuclear mechanisms [1, 3].

In neutrino physics, understanding nuclear effects is necessary for correct interpretation of measurements of electroweak parameters and evaluation of corresponding uncertainties [7]. The precision of modern neutrino oscillation experiments has rekindled interest in measuring nuclear effects, albeit at lower neutrino energies where elastic and resonance processes, rather than deep inelastic processes, are dominant [8].

Neutrino scattering, unlike that of charged leptons, involves the axial-vector current and is sensitive to specific quark and antiquark flavors. Therefore, nuclear modifications of neutrino cross sections may differ from those of charged leptons [9–12]. An indirect extraction of neutrino deep inelastic structure function ratios using NuTeV Fe [13] and CHORUS Pb [14] data suggests this is the case [15]. If confirmed, this either challenges the validity of QCD factorization for processes involving bound nucleons or signals inconsistency between neutrino and charged lepton data. Another study [16] using different techniques does not find this behavior. Neutrino scattering data are necessary for separation of valence and sea quark contributions to parton distribution functions [15, 17, 18], but high-statistics data from iron and lead must be corrected to account for poorly measured nuclear modifications.

Direct measurements of neutrino cross section ratios for different nuclei are therefore of significant interest and importance. So far, the only such measurements are ratios of Ne to D [19–21], but these are rarely used because of large statistical uncertainties and model-dependent extraction from a mixed H-Ne target. In this Letter, we report the first measurement of inclusive charged-current neutrino cross section ratios of C, Fe, and Pb to scintillator (CH) as functions of neutrino energy  $E_\nu$  and  $x$ . This is the first application to neutrino physics of the EMC-style technique of measuring nuclear dependence with multiple nuclear targets in the same beam and detector.

MINERvA uses a finely segmented detector to record interactions of neutrinos produced by the NuMI beam line [22] at Fermilab. Data for this analysis come from  $2.94 \times 10^{20}$  protons on target taken between March 2010 and April 2012 when the beam line produced a broadband neutrino beam peaked at 3.5 GeV with  $> 95\%$   $\nu_\mu$  at the peak energy. The MINERvA detector is comprised of 120 hexagonal modules perpendicular to the  $z$  axis, which is tilted 58 mrad upwards with respect to the beam line [23]. There are four module types: active tracking, electromagnetic calorimeter, hadronic calorimeter, and inactive nuclear target. The most upstream part of the detector includes five inactive targets, numbered from

upstream to downstream, each separated by four active tracking modules. Target 4 is lead; other targets comprise two or three materials arranged at differing transverse positions filling the  $x-y$  plane. Targets 1, 2, and 5 are constructed of steel and lead plates joined together; target 3 has graphite, steel, and lead plates. Total fiducial masses of C, Fe, and Pb in the nuclear target region are 0.159, 0.628, and 0.711 tons, respectively. A fully active tracking region with a fiducial mass of 5.48 tons is downstream of the nuclear target region. The target and tracker regions are surrounded by electromagnetic and hadronic calorimeters. The MINOS near detector, a magnetized iron spectrometer [24], is located 2 m downstream of the MINERvA detector.

Neutrino flux is predicted using a GEANT4-based simulation tuned to hadron production data [25] as described in Ref. [26]<sup>1</sup>. Neutrino interactions in the detector are simulated using GENIE 2.6.2 [27]. In GENIE, the initial nucleon momentum is selected from distributions in Refs. [28, 29]. Scattering kinematics are calculated in the (off-shell) nucleon rest frame. The quasielastic cross section is reduced to account for Pauli blocking. For quasielastic and resonance processes, free nucleon form factors are used. Quasielastic model details are given in Ref. [26]. Kinematics for nonresonant inelastic processes are selected from the model of Ref. [30] which effectively includes target mass and higher twist corrections. An empirical correction factor based on charged lepton deep inelastic scattering measurements of  $F_2^D/F_2^{(n+p)}$  and  $F_2^{Fe}/F_2^D$  is applied to all structure functions as a function of  $x$ , independent of the four-momentum transfer squared  $Q^2$  and  $A$ . This accounts for all nuclear effects except those related to neutron excess, which are applied separately.

The MINERvA detector’s response is simulated by a tuned GEANT4-based [31, 32] simulation. The energy scale of the detector is set by ensuring both detected photon statistics and reconstructed energy deposited by momentum-analyzed throughgoing muons agree in data and simulation. Calorimetric constants applied to reconstruct the recoil energy are determined by simulation. This procedure is cross-checked by comparing data and simulation of a scaled-down version of the MINERvA detector in a low energy hadron test beam [23].

Charged-current  $\nu_\mu$  events must have a reconstructed  $\mu^-$ . The muon is identified by a minimum ionizing track that traverses MINERvA [23] and travels downstream into the MINOS spectrometer [24] where its momentum and charge are measured. Muon selection and energy ( $E_\mu$ ) reconstruction are described in Refs. [23, 26, 33]. Requiring a matching track in MINOS restricts muon

<sup>1</sup> See Supplemental Material for a table of the simulated neutrino flux.

acceptance. To minimize acceptance differences across the MINERvA detector, the analysis requires neutrino energies above 2 GeV and muon angles with respect to the beam ( $\theta_\mu$ ) less than  $17^\circ$ . A 20 GeV upper limit on neutrino energy reduces the  $\bar{\nu}_\mu$  background to below 1%. After all selection criteria, 5953 events in C, 19024 in Fe, 23967 in Pb, and 189168 in CH are analyzed.

The event vertex is the location of the most upstream energy deposition on the muon track when only one track is reconstructed; a Kalman filter [34, 35] is used to fit the vertex position for events with multiple tracks. Between 10% and 20% of selected events in the different samples have a well-reconstructed multitrack vertex; the remainder are single track or have a poorly reconstructed vertex position based on the  $\chi^2$  of the vertex fit. Events with vertices in targets 2 through 5 and the fully active tracking volume are considered. The target 1 sample has a higher background from interactions upstream of the detector.

Events with a vertex in the active tracking region are divided into three statistically independent CH samples used to form ratios with C, Fe, and Pb. Events are associated with the C, Fe, or Pb of a nuclear target if the vertex position is between one plane upstream and two planes downstream of that nuclear target module and more than 2.5 cm away transversely from seams that join different materials in the target. In single-track events, the muon track is propagated to the longitudinal center of the nuclear target to estimate the vertex position and momentum of the muon. After all cuts, charged-current event selection efficiency ranges from 24% in the most upstream targets to 50% in the most downstream. The large efficiency variation exists because the upstream region has more inert material and smaller MINOS solid angle coverage.

Energy of the hadronic recoil system  $\nu$  is determined from the calorimetric sum of energy deposits not associated with the muon track. We consider deposits which occur between 20 ns before and 35 ns after the muon to reduce contributions from overlap with other neutrino interactions. Visible energies are weighted to account for the active fraction of scintillator in different regions of the detector. The overall calorimetric scale comes from fitting reconstructed  $\nu$  to generated  $\nu$  for simulated events in the active tracking region [23]. Using the same procedure, additional calorimetric scales for events in targets 2 through 5 are obtained as relative to the tracker; these are, respectively, 1.11, 1.04, 0.99, and 0.98.

Kinematic variables  $E_\nu$ ,  $x$ , and  $Q^2$  are obtained from reconstructed  $E_\mu$ ,  $\theta_\mu$ , and  $\nu$ :  $E_\nu = E_\mu + \nu$ ,  $Q^2 = 4E_\nu E_\mu \sin^2(\frac{\theta_\mu}{2})$ , and  $x = \frac{Q^2}{2M_N \nu}$ , where  $M_N$  is the average of proton and neutron masses. Reconstructed  $E_\nu$  distributions are corrected for detector smearing using iterative Bayesian unfolding [36] with four iterations to produce event yields as functions of unfolded  $E_\nu$ , with

generated  $E_\nu$  values from GENIE.

Reconstructed  $x$  is smeared broadly, especially at high  $x$  where quasielastic processes dominate. For these events, the hadronic recoil system can be a single nucleon, which is not reconstructed well under a calorimetric assumption. Such significant smearing would cause large uncertainties in the unfolding procedure. We therefore report cross section ratios as functions of reconstructed  $x^2$ .

Nuclear target samples contain events from adjacent tracking modules due to the loose cut on longitudinal vertex position. This background, called “CH contamination,” ranges from 20% to 40% and is roughly proportional to the ratio of areal densities of the target to surrounding scintillator. CH contamination is estimated by extrapolating event rates measured in the active tracking region to the nuclear target region. The tracking and nuclear target regions occupy different areas, and therefore have different acceptance into the MINOS detector. Further, the Fe and Pb targets in the nuclear target region stimulates greater activity in hadronic showers, which affects tracking efficiency. To account for the geometric acceptance difference, we apply a correction  $w^{t,A}(E_\mu, \theta_\mu)$ , obtained from a large, single-particle simulated  $\mu^-$  sample. Here  $t = 2, 3, 4, 5$  is the target number and  $A = C, Fe, Pb$  is the target nucleus. We account for  $\nu$ -dependent efficiency differences using simulated neutrino events to derive a correction  $w^{t,A}(\nu)$ . Differences are largest at low  $\nu$ . Acceptance- and efficiency-corrected distributions are scaled such that the integrated number of events in true and estimated backgrounds are equal according to neutrino event simulation. Figure 1 shows the  $x$  distribution of events passing all selection criteria in data and simulation; the estimated CH contamination is also shown.

Deviations found in simulated events between the estimated CH contamination by extrapolation and the predicted CH contamination using generator-level information are not fully covered by statistical uncertainty at the 68% confidence level in all targets. Additional systematic uncertainty is applied to ensure coverage at the 68% level. CH contamination uncertainties are 1%–8% from these systematic deviations and 2%–5% from statistics.

Small backgrounds from  $\bar{\nu}_\mu$  ( $< 0.4\%$ ) and neutral current ( $< 0.1\%$ ) events are estimated using simulation and subtracted. Transverse smearing within a nuclear target causes roughly 0.5% of the interactions to be assigned an incorrect target nucleus; this is also estimated by simulation and subtracted. A background from upstream neutrino interactions of  $6.2\% \pm 2.4\%$  exists only in target 2 for one third of the beam exposure, because two of the modules upstream of target 1 were not yet instrumented;

<sup>2</sup> See Supplemental Material for migration matrices necessary for comparisons of theoretical models to these data.

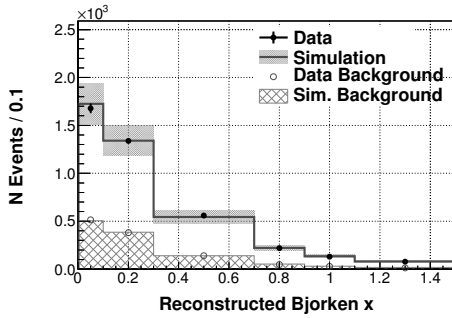


FIG. 1: Reconstructed Bjorken  $x$  distributions in data and simulation for selected inclusive  $\nu_\mu$  events in the lead of Target 2. The plot includes CH contamination separately estimated using data and simulated events in the tracker region. Both simulation distributions are normalized to the data by the number of events passing all event selection criteria. Events are scaled to a bin size of 0.1. Events with  $x$  greater than 1.5 are not shown.

Reconstructed $x$	I	II	III	IV	V	Mean Generated $Q^2$
	(%)	(%)	(%)	(%)	(%)	(GeV <sup>2</sup> )
0.0–0.1	11.3	42.5	5.9	19.2	15.7	0.23
0.1–0.3	13.6	36.4	16.7	9.1	23.0	0.70
0.3–0.7	32.7	32.8	11.8	1.4	21.1	1.00
0.7–0.9	55.1	25.4	4.3	0.5	14.6	0.95
0.9–1.1	62.7	21.6	2.8	0.5	12.3	0.90
1.1–1.5	69.6	18.1	1.9	0.4	9.9	0.82
> 1.5	79.1	12.8	0.6	0.3	7.1	0.86

TABLE I: Average sample composition of selected nuclear target and tracker events in reconstructed  $x$  bins based on GENIE simulation of different physics processes, together with the average generated  $Q^2$ . Processes are (I) quasielastic, (II) baryon resonance production, (III) deep inelastic scattering at  $Q^2 > 1$  GeV<sup>2</sup> and  $W > 2$  GeV, (IV) deep inelastic scattering at  $Q^2 < 1$  GeV<sup>2</sup> and  $W > 2$  GeV, and (V) nonresonant inelastic continuum with  $W < 2$  GeV.

affected data are weighted accordingly.

GENIE predicts a sample not dominated by any single process. Table I shows the predicted prevalence of processes in bins of reconstructed  $x$ . We compare GENIE’s prediction for inclusive cross section ratios restricted to  $2 < E_\nu < 20$  GeV and  $\theta_\mu < 17^\circ$  to two other models for nuclear modification of structure functions<sup>3</sup>. The Kulagin-Petti microphysical model starts with neutrino-nucleon structure functions and incorporates  $A$ -dependent nuclear effects [9, 37]. The updated Bodek-Yang treatment [38] of the model implemented in GENIE [30] includes an  $A$ -dependent empirical correction based on charged lepton measurements on the nuclei

<sup>3</sup> See Supplemental Material for a table summarizing the comparison of models of nuclear modification of inelastic structure functions.

$x$	I	II	III	IV	V	VI	Total
0.0–0.1	2.0	0.7	1.1	0.8	2.1	2.8	4.3
0.1–0.3	1.7	0.7	1.0	1.2	1.8	2.0	3.7
0.3–0.7	1.5	0.5	1.3	1.4	1.8	2.1	3.7
0.7–0.9	2.0	2.3	1.3	2.6	1.7	4.8	6.7
0.9–1.1	2.9	3.8	1.4	2.9	1.8	6.4	8.8
1.1–1.5	2.8	3.2	1.6	3.6	2.0	7.2	9.5

TABLE II: Systematic uncertainties (expressed as percentages) on the ratio of charged-current inclusive  $\nu_\mu$  differential cross sections  $\frac{d\sigma^{Fe}}{dx} / \frac{d\sigma^{CH}}{dx}$  with respect to  $x$  associated with (I) subtraction of CH contamination, (II) detector response to muons and hadrons, (III) neutrino interaction models, (IV) final state interaction models, (V) flux and target number, and (VI) statistics. The rightmost column shows the total uncertainty due to all sources.

of interest. Although nuclear structure functions vary by 20% among models, ratios of structure functions in Fe or Pb to C differ by  $\lesssim 1\%$ .

The total cross section for an  $E_\nu$  bin  $i$  is  $\sigma_i = \frac{\sum_j U_{ij}(N_j - N_j^{bg})}{\varepsilon_i T \Phi_i}$ , where  $U_{ij}$  is a matrix that accounts for smearing from true energy bin  $i$  to reconstructed energy bin  $j$ ;  $N_j$  and  $N_j^{bg}$  are the numbers of total and estimated background events in bin  $j$ , respectively;  $\varepsilon_i$  is the efficiency for reconstructing signal events in bin  $i$ ;  $T$  is the number of target nucleons; and  $\Phi_i$  is the neutrino flux bin  $i$ . The flux-integrated differential cross section for a reconstructed  $x$  bin  $j$  is  $(\frac{d\sigma}{dx})_j = \frac{N_j - N_j^{bg}}{\varepsilon_j T \Phi \Delta_j(x)}$ , where  $\Phi$  is the neutrino flux integrated from 2 to 20 GeV,  $\Delta_j(x)$  is bin width, and other terms have the same meaning as above. No correction is applied to account for neutron excess in any target nuclei.

The main sources of systematic uncertainty in the cross section ratio measurements are (I) subtraction of CH contamination; (II) detector response to muons and hadrons; (III) neutrino interaction models; (IV) final state interaction models; and (V) target number. Uncertainty in flux is considered but negligible. All uncertainties are evaluated by repeating the cross section analysis with systematic shifts applied to simulation. Muon and recoil energy reconstruction uncertainties are described in Ref. [26] and Ref. [33], respectively. We evaluate systematic error from cross section and final state interaction models by varying underlying model parameters in GENIE within their uncertainties [27]. Since variations in model parameters affect calorimetric scale factors, these are reextracted during systematic error evaluation. Recoil energy and final state interaction model uncertainties increase with  $x$ , because interactions of lower energy hadrons are not as well constrained. An assay of detector components yields an uncertainty in scintillator, carbon, iron, and lead masses of 1.4%, 0.5%, 1.0%, and 0.5%, respectively. The resulting uncertainties on  $\frac{d\sigma^{Fe}}{dx} / \frac{d\sigma^{CH}}{dx}$

are shown in Table II<sup>4</sup>.

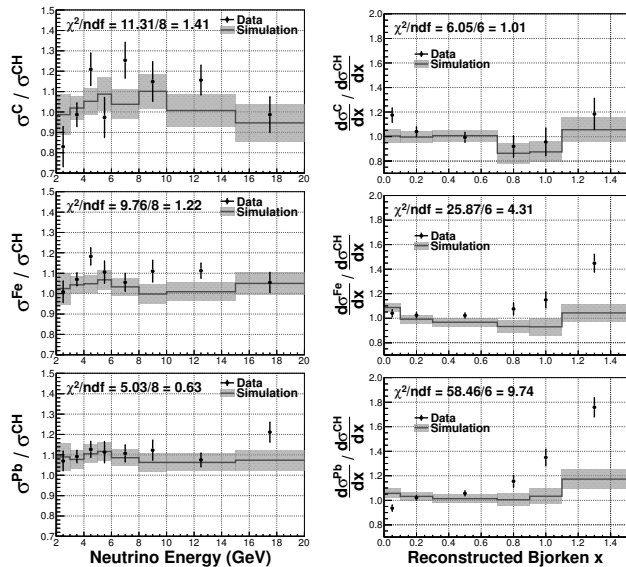


FIG. 2: Ratios of the charged-current inclusive  $\nu_\mu$  cross section per nucleon as a function of  $E_\nu$  (left) and as a function of reconstructed  $x$  (right) for C/CH (top), Fe/CH (middle), and Pb/CH (bottom). Error bars on the data (simulation) show the statistical (systematic) uncertainties. The  $\chi^2$  calculation includes correlations among all bins shown. Events with  $x$  greater than 1.5 are not shown.

Ratios of charged-current  $\nu_\mu$  cross sections per nucleon  $\sigma(E_\nu)$  and  $\frac{d\sigma}{dx}$  are shown in Fig. 2<sup>5</sup>. Simulation reproduces these measurements within roughly 10%. In contrast, measurements of  $\frac{d\sigma^A}{dx} / \frac{d\sigma^{\text{CH}}}{dx}$  show a suppression of the ratio compared to simulation at low  $x$  and an enhancement at high  $x$ , both of which increase with the size of the nucleus.

Low  $x$  bins are expected to show shadowing, which lowers the cross section for heavier nuclei [12, 39, 40]. Shadowing in these data may be larger than predicted for several reasons. First, our data are at low  $Q^2$  in the nonperturbative range (80% of events below  $1.0 \text{ GeV}^2$  and 60% below  $0.5 \text{ GeV}^2$ ), while the model is tuned to data at much higher  $Q^2$  where shadowing is well measured. Second, shadowing in the model is assumed to be the same for C and Pb and equal to measurements from Fe [30]. Finally, the shadowing model used for comparison is based on charged lepton data, which do not have axial-vector contributions. The array of nuclear models available to modern neutrino experiments give similar results for these cross section ratios; none of which is

confirmed by the data.

Higher  $x$  bins contain mostly (>63%) quasielastic events, whose rates may be enhanced by meson-exchange currents [41–47], which are not in the simulation. The excess observed here may be related to the excess in MINOS Fe data at low inelasticity compared to a simulation with nuclear corrections based on lighter nuclei similar to GENIE’s [48, 49]. The failure of nuclear scaling models in this region has profound implications for neutrino oscillation experiments that utilize quasielastic events. For example, T2K [50, 51] must apply a nuclear model to relate the rate in the carbon of a near detector to oxygen in the far detector. LBNE [52] must extrapolate existing data on C, Fe, Pb to Ar. Until better models exist that cover the relevant kinematic domain, oscillation experiments must incorporate the discrepancies measured here in evaluating systematic uncertainties. More theoretical work is needed to correctly model nuclear effects in neutrino interactions, from the quasielastic to the deep inelastic regime.

This work was supported by the Fermi National Accelerator Laboratory under U.S. Department of Energy Contract No. DE-AC02-07CH11359 which included the MINERvA construction project. Construction support also was granted by the United States National Science Foundation under Grant No. PHY-0619727 and by the University of Rochester. Support for participating scientists was provided by NSF and DOE (USA) by CAPES and CNPq (Brazil), by CoNaCyT (Mexico), by CONICYT (Chile), by CONCYTEC, DGI-PUCP and IDI/IGI-UNI (Peru), by Latin American Center for Physics (CLAF), by the Swiss National Science Foundation, and by RAS and the Russian Ministry of Education and Science (Russia). We thank the MINOS Collaboration for use of its near detector data. Finally, we thank the staff of Fermilab for support of the beam line and detector.

\* now at Argonne National Laboratory, Argonne, IL 60439, USA

† now at Vrije Universiteit Brussel, Pleinlaan 2, B-1050 Brussels, Belgium

‡ also at Department of Physics, University of Antananarivo, Madagascar

- [1] M. Arneodo, Phys. Rep. **240**, 301 (1994).
- [2] D. F. Geesaman, K. Saito, and A. W. Thomas, Annu. Rev. Nucl. Part. Sci. **45**, 337 (1995).
- [3] P. Norton, Rept. Prog. Phys. **66**, 1253 (2003).
- [4] K. Rith, (2014), arXiv:1402.5000.
- [5] J. J. Aubert *et al.* (European Muon Collaboration), Phys. Lett. B **123**, 275 (1983).
- [6] J. J. Aubert *et al.* (European Muon Collaboration), Nucl. Phys. B **293**, 740 (1987).
- [7] G. P. Zeller *et al.* (NuTeV Collaboration), Phys. Rev. Lett. **88**, 091802 (2002), arXiv:0110059 [hep-ex].

<sup>4</sup> See Supplemental Material for uncertainties on all cross section ratios as functions of  $E_\nu$  and  $x$ .

<sup>5</sup> See Supplemental Material for cross section ratio measurements compared to simulation in tabular form and correlations of uncertainties among bins.

- [8] P. Coloma, P. Huber, C.-M. Jen, and C. Mariani, *Phys. Rev. D* **89**, 073015 (2014), arXiv:1311.4506 .
- [9] S. A. Kulagin and R. Petti, *Nucl. Phys. A* **765**, 126 (2006), arXiv:0412425 [hep-ph] .
- [10] H. Haider, I. R. Simo, M. S. Athar, and M. J. Vicente Vacas, *Phys. Rev. C* **84**, 054610 (2011).
- [11] H. Haider, I. R. Simo, and M. S. Athar, (2013), arXiv:1303.5927 [nucl-th] .
- [12] B. Z. Kopeliovich, J. G. Morfin, and I. Schmidt, *Prog. Part. Nucl. Phys.* **68**, 314 (2013), arXiv:1208.6541 [hep-ph] .
- [13] M. Tzanov *et al.* (NuTeV Collaboration), *Phys. Rev. D* **74**, 012008 (2006).
- [14] G. Önençüt *et al.* (CHORUS Collaboration), *Phys. Lett. B* **632**, 65 (2006).
- [15] K. Kovarik, I. Schienbein, F. I. Olness, J. Y. Yu, C. Keppel, J. G. Morfin, J. F. Owens, and T. Stavreva, *Phys. Rev. Lett.* **106**, 122301 (2011), arXiv:1012.0286 [hep-ph] .
- [16] H. Paukkunen and C. A. Salgado, *Phys. Rev. Lett.* **110**, 212301 (2013).
- [17] M. Hirai, S. Kumano, and T.-H. Nagai, *Phys. Rev. C* **76**, 065207 (2007).
- [18] I. Schienbein, J. Y. Yu, C. Keppel, J. G. Morfin, F. Olness, and J. F. Owens, *Phys. Rev. D* **77**, 054013 (2008).
- [19] M. A. Parker *et al.* (BEBC TST Neutrino Collaboration), *Nucl. Phys. B* **232**, 1 (1984).
- [20] A. M. Cooper-Sarkar *et al.* (WA25 and WA59 Collaborations), *Phys. Lett. B* **141**, 133 (1984).
- [21] J. Hanlon *et al.*, *Phys. Rev. D* **32**, 2441 (1985).
- [22] K. Anderson *et al.*, FERMILAB-DESIGN-1998-01 (1998).
- [23] L. Aliaga *et al.* (MINERvA Collaboration), *Nucl. Instrum. Methods Phys. Res., Sect. A* **743**, 130 (2014), arXiv:1305.5199 [physics.ins-det] .
- [24] D. Michael *et al.* (MINOS Collaboration), *Nucl. Instrum. Methods Phys. Res., Sect. A* **596**, 190 (2008), arXiv:0805.3170 .
- [25] C. Alt *et al.* (NA49 Collaboration), *Eur. Phys. J. C* **49**, 897 (2007), arXiv:0606028 [hep-ex] .
- [26] L. Fields *et al.* (MINERvA Collaboration), *Phys. Rev. Lett.* **111**, 022501 (2013), arXiv:1305.2234 [hep-ex] .
- [27] C. Andreopoulos *et al.* (GENIE Collaboration), *Nucl. Instrum. Methods Phys. Res., Sect. A* **614**, 87 (2010), Program version 2.6.2 used here, arXiv:0905.2517 [hep-ph] .
- [28] A. Bodek and J. L. Ritchie, *Phys. Rev. D* **23**, 1070 (1981).
- [29] A. Bodek and J. L. Ritchie, *Phys. Rev. D* **24**, 1400 (1981).
- [30] A. Bodek, I. Park, and U.-K. Yang, *Nucl. Phys. Proc. Suppl.* **139**, 113 (2005), arXiv:0411202 [hep-ph] .
- [31] S. Agostinelli *et al.*, *Nucl. Instrum. Methods Phys. Res., Sect. A* **506**, 250 (2003).
- [32] J. Allison *et al.*, *IEEE Trans. Nucl. Sci.* **53**, 270 (2006).
- [33] G. Fiorentini *et al.* (MINERvA Collaboration), *Phys. Rev. Lett.* **111**, 022502 (2013), arXiv:1305.2243 [hep-ex] .
- [34] R. Frühwirth, *Nucl. Instrum. Methods Phys. Res., Sect. A* **262**, 444 (1987).
- [35] R. Luchsinger and C. Grab, *Comput. Phys. Commun.* **76**, 263 (1993).
- [36] G. D’Agostini, *Nucl. Instrum. Methods Phys. Res., Sect. A* **362**, 487 (1995).
- [37] S. A. Kulagin and R. Petti, *Phys. Rev. D* **76**, 094023 (2007), arXiv:0703033 [hep-ph] .
- [38] A. Bodek and U. K. Yang, (2013), arXiv:1011.6592v2 .
- [39] M. Adams *et al.* (E665 Collaboration), *Z. Phys. C* **67**, 403 (1995), arXiv:9505006 [hep-ex] .
- [40] P. P. Allport *et al.* (BEBC WA59 Collaboration), *Phys. Lett. B* **232**, 417 (1989).
- [41] J. Carlson, J. Jourdan, R. Schiavilla, and I. Sick, *Phys. Rev. C* **65**, 024002 (2002), arXiv:0106047 .
- [42] M. Martini, M. Ericson, G. Chanfray, and J. Marteau, *Phys. Rev. C* **80**, 065501 (2009).
- [43] M. Martini, M. Ericson, G. Chanfray, and J. Marteau, *Phys. Rev. C* **81**, 045502 (2010).
- [44] A. Bodek, H. S. Budd, and M. E. Christy, *Eur. Phys. J. C* **71**, 1726 (2011), arXiv:1106.0340 [hep-ph] .
- [45] J. E. Amaro, M. B. Barbaro, J. A. Caballero, T. W. Donnelly, and C. F. Williamson, *Phys. Lett. B* **696**, 151 (2011), arXiv:1010.1708 [nucl-th] .
- [46] J. Nieves, I. R. Simo, and M. J. Vicente Vacas, *Phys. Rev. C* **83**, 045501 (2011), arXiv:1102.2777 [hep-ph] .
- [47] R. Gran, J. Nieves, F. Sanchez, and M. J. Vicente Vacas, *Phys. Rev. D* **88**, 113007 (2013), arXiv:1307.8105 [hep-ph] .
- [48] P. Adamson *et al.* (MINOS Collaboration), *Phys. Rev. D* **77**, 072002 (2008).
- [49] P. Adamson *et al.* (MINOS Collaboration), (2007), arXiv:0708.1495 .
- [50] K. Abe *et al.* (T2K Collaboration), *Phys. Rev. Lett.* **111**, 211803 (2013).
- [51] K. Abe *et al.* (T2K Collaboration), *Phys. Rev. Lett.* **112**, 061802 (2014).
- [52] C. Adams *et al.* (LBNE Collaboration), (2014), arXiv:1307.7335v3 .

## SUPPLEMENTAL MATERIAL

	$x$ Bin	Data	Sim.	$\sigma_{stat}$	$\sigma_{sys}$	$\frac{(\text{Data}-\text{Sim.})}{\sigma}$
Carbon	0.0–0.1	1.17	1.01	0.056	0.056	2.01
	0.1–0.3	1.04	1.00	0.038	0.039	0.76
	0.3–0.7	0.99	1.01	0.039	0.038	-0.25
	0.7–0.9	0.92	0.86	0.087	0.072	0.46
	0.9–1.1	0.96	0.88	0.111	0.066	0.58
	1.1–1.5	1.18	1.06	0.126	0.089	0.79
Iron	0.0–0.1	1.04	1.09	0.028	0.032	-1.02
	0.1–0.3	1.02	0.99	0.020	0.031	0.83
	0.3–0.7	1.02	0.97	0.021	0.032	1.37
	0.7–0.9	1.08	0.93	0.048	0.053	1.91
	0.9–1.1	1.15	0.93	0.064	0.075	2.14
	1.1–1.5	1.45	1.04	0.072	0.086	3.51
Lead	0.0–0.1	0.94	1.06	0.025	0.029	-2.99
	0.1–0.3	1.02	1.03	0.018	0.030	-0.32
	0.3–0.7	1.06	1.01	0.020	0.034	1.09
	0.7–0.9	1.15	1.00	0.047	0.051	2.06
	0.9–1.1	1.35	1.03	0.067	0.070	3.16
	1.1–1.5	1.76	1.17	0.077	0.103	4.45

TABLE III: Comparison of measured values to simulation predictions for  $\frac{d\sigma^A}{dx} / \frac{d\sigma^{CH}}{dx}$  for each  $x$  bin.

	$E_\nu$ Bin (GeV)	Data	Sim.	$\sigma_{stat}$	$\sigma_{sys}$	$\frac{(\text{Data}-\text{Sim.})}{\sigma}$
Carbon	2-3	0.83	0.99	0.096	0.072	-1.23
	3-4	0.99	1.02	0.056	0.051	-0.41
	4-5	1.21	1.05	0.077	0.063	1.51
	5-6	0.97	1.09	0.096	0.058	-0.95
	6-8	1.25	1.04	0.084	0.070	1.85
	8-10	1.15	1.10	0.093	0.068	0.38
	10-15	1.16	1.01	0.069	0.075	1.36
	15-20	0.99	0.95	0.084	0.076	0.33
Iron	2-3	1.01	1.02	0.051	0.072	-0.17
	3-4	1.07	1.04	0.031	0.041	0.50
	4-5	1.18	1.05	0.041	0.043	2.17
	5-6	1.11	1.07	0.052	0.042	0.54
	6-8	1.06	1.03	0.042	0.038	0.37
	8-10	1.11	1.00	0.051	0.043	1.57
	10-15	1.11	1.01	0.035	0.043	1.73
	15-20	1.05	1.05	0.046	0.049	0.06
Lead	2-3	1.07	1.09	0.046	0.062	-0.25
	3-4	1.09	1.08	0.029	0.042	0.27
	4-5	1.13	1.10	0.038	0.042	0.37
	5-6	1.11	1.12	0.050	0.039	-0.05
	6-8	1.11	1.09	0.040	0.035	0.38
	8-10	1.12	1.06	0.047	0.039	0.91
	10-15	1.08	1.06	0.032	0.038	0.23
	15-20	1.21	1.07	0.046	0.048	1.92

TABLE IV: Comparison of measured values to simulation predictions for  $\sigma^A/\sigma^{CH}$  for each  $E_\nu$  bin.

Target	Mass (ton)	Protons ( $\times 10^{30}$ )	Neutrons ( $\times 10^{30}$ )	Nucleons ( $\times 10^{30}$ )	Uncertainty %
C	0.159	0.048	0.048	0.096	1.4
Fe	0.628	0.176	0.203	0.379	0.5
Pb	0.711	0.169	0.258	0.427	1.0
CH	5.476	1.760	1.534	3.294	0.5

TABLE V: Mass and uncertainty on mass; and number of protons, neutrons, and the total target nucleons in the fiducial volume for each nuclear target.

$E_\nu$ in Bin (GeV)	2-2.5	2.5-3	3-3.5	3.5-4	4-4.5	4.5-5	5-5.5	5.5-6	6-6.5
$\nu_\mu$ Flux (neutrinos/cm <sup>2</sup> /POT) $\times 10^{-8}$	0.409	0.501	0.526	0.419	0.253	0.137	0.080	0.055	0.042
$E_\nu$ in Bin (GeV)	6.5-7	7-7.5	7.5-8	8-8.5	8.5-9	9-9.5	9.5-10	10-11	11-12
$\nu_\mu$ Flux (neutrinos/cm <sup>2</sup> /POT) $\times 10^{-8}$	0.036	0.030	0.027	0.024	0.021	0.019	0.017	0.030	0.025
$E_\nu$ in Bin (GeV)	12-13	13-14	14-15	15-16	16-17	17-18	18-19	19-20	
$\nu_\mu$ Flux (neutrinos/cm <sup>2</sup> /POT) $\times 10^{-8}$	0.021	0.018	0.015	0.012	0.010	0.009	0.007	0.006	

TABLE VI: The calculated muon neutrino flux per proton on target (POT) for the data included in the analysis.



$x$ bin	0.0–0.1	0.1–0.3	0.3–0.7	0.7–0.9	0.9–1.1	1.1–1.5
Ratio of cross sections	1.175	1.040	0.993	0.919	0.956	1.184
Error on ratio	$\pm 0.074$	$\pm 0.054$	$\pm 0.055$	$\pm 0.110$	$\pm 0.126$	$\pm 0.149$
$x$ bin						
0.0–0.1	1.000	0.329	0.264	0.099	0.140	0.128
0.1–0.3		1.000	0.338	0.152	0.162	0.148
0.3–0.7			1.000	0.172	0.165	0.172
0.7–0.9				1.000	0.046	-0.020
0.9–1.1					1.000	0.123
1.1–1.5						1.000

TABLE VII: Measured ratio of charged-current inclusive  $\nu_\mu$  differential cross sections  $\frac{d\sigma^C}{dx} / \frac{d\sigma^{CH}}{dx}$  with respect to  $x$ , their total (statistical and systematic) uncertainties, and the correlation matrix for these uncertainties.

$x$ bin	0.0–0.1	0.1–0.3	0.3–0.7	0.7–0.9	0.9–1.1	1.1–1.5
Ratio of cross sections	1.041	1.024	1.022	1.076	1.150	1.449
Error on ratio	$\pm 0.043$	$\pm 0.037$	$\pm 0.037$	$\pm 0.067$	$\pm 0.088$	$\pm 0.095$
$x$ bin						
0.0–0.1	1.000	0.525	0.457	0.247	0.262	0.256
0.1–0.3		1.000	0.534	0.243	0.341	0.290
0.3–0.7			1.000	0.393	0.377	0.372
0.7–0.9				1.000	0.128	0.204
0.9–1.1					1.000	0.359
1.1–1.5						1.000

TABLE VIII: Measured ratio of charged-current inclusive  $\nu_\mu$  differential cross sections  $\frac{d\sigma^{Fe}}{dx} / \frac{d\sigma^{CH}}{dx}$  with respect to  $x$ , their total (statistical and systematic) uncertainties, and the correlation matrix for these uncertainties.

$x$ bin	0.0–0.1	0.1–0.3	0.3–0.7	0.7–0.9	0.9–1.1	1.1–1.5
Ratio of cross sections	0.936	1.021	1.057	1.155	1.350	1.758
Error on ratio	$\pm 0.041$	$\pm 0.035$	$\pm 0.038$	$\pm 0.065$	$\pm 0.085$	$\pm 0.103$
$x$ bin						
0.0–0.1	1.000	0.592	0.486	0.332	0.271	0.257
0.1–0.3		1.000	0.608	0.415	0.345	0.309
0.3–0.7			1.000	0.445	0.393	0.389
0.7–0.9				1.000	0.262	0.289
0.9–1.1					1.000	0.325
1.1–1.5						1.000

TABLE IX: Measured ratio of charged-current inclusive  $\nu_\mu$  differential cross sections  $\frac{d\sigma^{Pb}}{dx} / \frac{d\sigma^{CH}}{dx}$  with respect to  $x$ , their total (statistical and systematic) uncertainties, and the correlation matrix for these uncertainties.

$E_\nu$ (GeV) bin	2–3	3–4	4–5	5–6	6–8	8–10	10–15	15–20
Ratio of cross sections	0.830	0.987	1.210	0.973	1.254	1.149	1.157	0.987
Error on ratio	$\pm 0.128$	$\pm 0.077$	$\pm 0.095$	$\pm 0.115$	$\pm 0.102$	$\pm 0.114$	$\pm 0.095$	$\pm 0.111$
$E_\nu$ (GeV) bin								
2–3	1.000	0.272	0.180	0.051	0.107	0.052	0.117	0.046
3–4		1.000	0.281	0.193	0.181	0.156	0.197	0.169
4–5			1.000	0.149	0.191	0.112	0.202	0.174
5–6				1.000	0.090	0.156	0.177	0.153
6–8					1.000	0.104	0.211	0.191
8–10						1.000	0.193	0.179
10–15							1.000	0.280
15–20								1.000

TABLE X: Measured ratio of charged-current inclusive  $\nu_\mu$  total cross sections  $\sigma^C / \sigma^{CH}$  as a function of  $E_\nu$ , their total (statistical and systematic) uncertainties, and the correlation matrix for these uncertainties.

$E_\nu$ (GeV) bin	2-3	3-4	4-5	5-6	6-8	8-10	10-15	15-20
Ratio of cross sections	1.009	1.070	1.183	1.106	1.056	1.110	1.113	1.055
Error on ratio	$\pm 0.089$	$\pm 0.051$	$\pm 0.056$	$\pm 0.066$	$\pm 0.056$	$\pm 0.064$	$\pm 0.053$	$\pm 0.067$
$E_\nu$ (GeV) bin								
2-3	1.000	0.381	0.219	0.239	0.095	0.122	0.105	0.003
3-4		1.000	0.450	0.352	0.284	0.200	0.207	0.120
4-5			1.000	0.291	0.282	0.217	0.224	0.166
5-6				1.000	0.221	0.190	0.235	0.161
6-8					1.000	0.224	0.299	0.298
8-10						1.000	0.298	0.228
10-15							1.000	0.340
15-20								1.000

TABLE XI: Measured ratio of charged-current inclusive  $\nu_\mu$  total cross sections  $\sigma^{Fe}/\sigma^{CH}$  as a function of  $E_\nu$ , their total (statistical and systematic) uncertainties, and the correlation matrix for these uncertainties.

$E_\nu$ (GeV) bin	2-3	3-4	4-5	5-6	6-8	8-10	10-15	15-20
Ratio of cross sections	1.070	1.092	1.127	1.113	1.107	1.123	1.075	1.212
Error on ratio	$\pm 0.078$	$\pm 0.050$	$\pm 0.056$	$\pm 0.063$	$\pm 0.053$	$\pm 0.060$	$\pm 0.050$	$\pm 0.062$
$E_\nu$ (GeV) bin								
2-3	1.000	0.465	0.275	0.262	0.168	0.139	0.080	0.091
3-4		1.000	0.506	0.376	0.330	0.203	0.197	0.134
4-5			1.000	0.348	0.338	0.234	0.259	0.194
5-6				1.000	0.265	0.214	0.216	0.194
6-8					1.000	0.252	0.317	0.249
8-10						1.000	0.329	0.273
10-15							1.000	0.365
15-20								1.000

TABLE XII: Measured ratio of charged-current inclusive  $\nu_\mu$  total cross sections  $\sigma^{Pb}/\sigma^{CH}$  as a function of  $E_\nu$ , their total (statistical and systematic) uncertainties, and the correlation matrix for these uncertainties.

$x$	I	II	III	IV	V	VI	Total
0.0–0.1	3.5	1.1	0.9	2.1	2.1	5.6	7.4
0.1–0.3	2.8	0.6	0.9	1.4	1.8	3.8	5.4
0.3–0.7	2.3	0.8	1.6	1.8	1.7	3.9	5.5
0.7–0.9	3.0	4.8	1.6	3.0	1.6	8.7	11.0
0.9–1.1	3.4	2.5	1.6	3.5	2.0	11.1	12.6
1.1–1.5	3.2	5.7	2.2	3.0	2.5	12.6	14.9

TABLE XIII: Systematic uncertainties (expressed as percentages) on the ratio of charged-current inclusive  $\nu_\mu$  differential cross sections  $\frac{d\sigma^C}{dx} / \frac{d\sigma^{CH}}{dx}$  with respect to  $x$  associated with (I) subtraction of CH contamination, (II) detector response to muons and hadrons, (III) neutrino interactions, (IV) final state interactions, (V) flux and target number, and (VI) statistics. The rightmost column shows the total uncertainty due to all sources.

$x$	I	II	III	IV	V	VI	Total
0.0–0.1	2.0	0.7	1.1	0.8	2.1	2.8	4.3
0.1–0.3	1.7	0.7	1.0	1.2	1.8	2.0	3.7
0.3–0.7	1.5	0.5	1.3	1.4	1.8	2.1	3.7
0.7–0.9	2.0	2.3	1.3	2.6	1.7	4.8	6.7
0.9–1.1	2.9	3.8	1.4	2.9	1.8	6.4	8.8
1.1–1.5	2.8	3.2	1.6	3.6	2.0	7.2	9.5

TABLE XIV: Systematic uncertainties (expressed as percentages) on the ratio of charged-current inclusive  $\nu_\mu$  differential cross sections  $\frac{d\sigma^{Fc}}{dx} / \frac{d\sigma^{CH}}{dx}$  with respect to  $x$  associated with (I) subtraction of CH contamination, (II) detector response to muons and hadrons, (III) neutrino interactions, (IV) final state interactions, (V) flux and target number, and (VI) statistics. The rightmost column shows the total uncertainty due to all sources.

$x$	I	II	III	IV	V	VI	Total
0.0–0.1	2.2	0.7	1.0	1.1	1.8	2.5	4.1
0.1–0.3	1.9	0.7	1.1	1.1	1.6	1.8	3.5
0.3–0.7	1.6	0.7	1.5	1.6	1.6	2.0	3.8
0.7–0.9	2.5	1.5	1.5	2.5	1.7	4.7	6.5
0.9–1.1	2.6	2.5	1.6	2.8	2.1	6.7	8.5
1.1–1.5	3.0	3.5	1.9	4.2	1.9	7.7	10.3

TABLE XV: Systematic uncertainties (expressed as percentages) on the ratio of charged-current inclusive  $\nu_\mu$  differential cross sections  $\frac{d\sigma^{Pb}}{dx} / \frac{d\sigma^{CH}}{dx}$  with respect to  $x$  associated with (I) subtraction of CH contamination, (II) detector response to muons and hadrons, (III) neutrino interactions, (IV) final state interactions, (V) flux and target number, and (VI) statistics. The rightmost column shows the total uncertainty due to all sources.

$E_\nu$ (GeV)	I	II	III	IV	V	VI	Total
2–3	3.4	5.2	4.2	2.6	3.1	9.6	12.8
3–4	3.1	1.0	2.7	2.2	2.2	5.6	7.7
4–5	3.4	1.6	2.3	2.3	2.3	7.7	9.5
5–6	4.0	3.0	2.1	1.9	2.9	9.6	11.5
6–8	3.9	2.4	1.9	1.5	2.6	8.4	10.2
8–10	4.6	2.3	2.1	1.4	3.1	9.3	11.4
10–15	5.2	1.2	1.9	2.0	2.6	6.9	9.5
15–20	5.9	1.6	1.9	1.7	2.9	8.4	11.1

TABLE XVI: Systematic uncertainties (expressed as percentages) on the ratio of charged-current inclusive  $\nu_\mu$  total cross sections  $\sigma^C / \sigma^{CH}$  as a function of  $E_\nu$  associated with (I) subtraction of CH contamination, (II) detector response to muons and hadrons, (III) neutrino interactions, (IV) final state interactions, (V) flux and target number, and (VI) statistics. The rightmost column shows the total uncertainty due to all sources.

$E_\nu$ (GeV)	I	II	III	IV	V	VI	Total
2–3	1.7	5.1	3.9	1.8	2.3	5.1	8.9
3–4	1.5	0.5	2.5	1.8	2.0	3.1	5.1
4–5	1.7	0.9	1.9	1.7	2.1	4.1	5.6
5–6	2.0	1.2	1.8	1.5	2.3	5.2	6.6
6–8	2.0	1.4	1.5	1.1	2.2	4.2	5.6
8–10	2.2	0.9	1.7	1.1	2.3	5.1	6.4
10–15	2.2	0.6	2.0	1.0	2.2	3.5	5.3
15–20	2.9	1.5	2.2	1.3	2.5	4.6	6.7

TABLE XVII: Systematic uncertainties (expressed as percentages) on the ratio of charged-current inclusive  $\nu_\mu$  total cross sections  $\sigma^{Fe}/\sigma^{CH}$  as a function of  $E_\nu$  associated with (I) subtraction of CH contamination, (II) detector response to muons and hadrons, (III) neutrino interactions, (IV) final state interactions, (V) flux and target number, and (VI) statistics. The rightmost column shows the total uncertainty due to all sources.

$E_\nu$ (GeV)	I	II	III	IV	V	VI	Total
2–3	1.5	3.8	3.7	2.0	2.1	4.6	7.8
3–4	1.4	0.5	2.8	1.9	1.8	2.9	5.0
4–5	2.0	1.0	2.2	1.8	1.9	3.8	5.6
5–6	1.9	1.0	1.9	1.6	2.1	5.0	6.3
6–8	1.8	0.7	1.6	1.2	2.0	4.0	5.3
8–10	2.0	0.6	1.7	1.3	2.1	4.7	6.0
10–15	2.3	0.9	1.8	0.8	2.0	3.2	5.0
15–20	2.6	0.8	2.1	0.8	2.2	4.6	6.2

TABLE XVIII: Systematic uncertainties (expressed as percentages) on the ratio of charged-current inclusive  $\nu_\mu$  total cross sections  $\sigma^{Pb}/\sigma^{CH}$  as a function of  $E_\nu$  associated with (I) subtraction of CH contamination, (II) detector response to muons and hadrons, (III) neutrino interactions, (IV) final state interactions, (V) flux and target number, and (VI) statistics. The rightmost column shows the total uncertainty due to all sources.

$x$ bin	0.0–0.1	0.1–0.3	0.3–0.7	0.7–0.9	0.9–1.1	1.1–1.5	overflow
0.0–0.1	73	23	3	0	0	0	0
0.1–0.3	12	60	23	2	1	1	2
0.3–0.7	4	20	47	9	5	6	9
0.7–0.9	2	11	30	11	9	10	26
0.9–1.1	2	8	30	12	6	10	31
1.1–1.5	3	7	21	8	8	14	38

TABLE XIX: Fractional bin migration in variable  $x$  for the carbon sample as predicted by simulation. The value of the bin is the percent of events that were generated in an  $x$  bin (row) that were reconstructed into an  $x$  bin (column).

$x$ bin	0.0–0.1	0.1–0.3	0.3–0.7	0.7–0.9	0.9–1.1	1.1–1.5	overflow
0.0–0.1	73	23	3	0	0	0	0
0.1–0.3	12	58	23	2	1	1	2
0.3–0.7	3	18	47	10	6	6	9
0.7–0.9	2	7	31	12	9	12	27
0.9–1.1	2	6	23	12	9	15	34
1.1–1.5	2	5	16	10	9	14	44

TABLE XX: Fractional bin migration in variable  $x$  for the iron sample as predicted by simulation. The value of the bin is the percent of events that were generated in an  $x$  bin (row) that were reconstructed into an  $x$  bin (column).

$x$ bin	0.0–0.1	0.1–0.3	0.3–0.7	0.7–0.9	0.9–1.1	1.1–1.5	overflow
0.0–0.1	72	24	4	0	0	0	0
0.1–0.3	12	59	23	2	1	1	1
0.3–0.7	3	19	47	10	6	6	9
0.7–0.9	2	8	29	13	10	12	25
0.9–1.1	2	6	23	12	11	13	33
1.1–1.5	2	5	16	11	8	14	44

TABLE XXI: Fractional bin migration in variable  $x$  for the lead sample as predicted by simulation. The value of the bin is the percent of events that were generated in an  $x$  bin (row) that were reconstructed into an  $x$  bin (column).

$x$ bin	0.0–0.1	0.1–0.3	0.3–0.7	0.7–0.9	0.9–1.1	1.1–1.5	overflow
0.0–0.1	75	22	2	0	0	0	0
0.1–0.3	10	66	21	1	1	1	1
0.3–0.7	2	15	59	11	5	4	3
0.7–0.9	2	5	33	21	14	13	12
0.9–1.1	2	4	19	19	17	19	20
1.1–1.5	1	4	12	12	14	24	33

TABLE XXII: Fractional bin migration in variable  $x$  for the scintillator sample as predicted by simulation. The value of the bin is the percent of events that were generated in an  $x$  bin (row) that were reconstructed into an  $x$  bin (column).

$x$	C/CH				Fe/CH				Pb/CH			
	G	$\sigma_{st}$	KP	BY	G	$\sigma_{st}$	KP	BY	G	$\sigma_{st}$	KP	BY
	%	%	$\Delta\%$	$\Delta\%$	%	%	$\Delta\%$	$\Delta\%$	%	%	$\Delta\%$	$\Delta\%$
0.0–0.1	1.050	1.0	0.3	0.0	1.011	0.5	-0.4	1.2	1.037	0.5	-1.5	0.8
0.1–0.3	1.034	0.7	-0.3	0.0	1.017	0.3	-0.7	-0.5	1.071	0.3	-1.0	-0.7
0.3–0.7	1.049	0.8	-0.1	0.0	1.049	0.4	0.0	0.0	1.146	0.4	0.4	0.6
0.7–0.9	1.089	1.8	-0.1	0.0	0.995	0.9	0.4	0.1	1.045	0.9	0.1	0.7
0.9–1.1	1.133	2.3	-0.1	0.0	0.948	1.1	0.2	0.0	0.985	1.1	0.2	0.2
1.1–1.5	1.111	2.2	0.0	0.0	0.952	1.1	0.0	0.0	1.036	1.1	0.1	0.0

TABLE XXIII: Predictions for charged-current cross section per nucleon ratios with  $2 < E_\nu < 20$  GeV and  $\theta_\mu < 17^\circ$  from GENIE (G) [30] with associated statistical uncertainty. Also shown is the deviation from GENIE predicted by the Kulagin-Petti (KP) [9, 37] and updated Bodek-Yang (BY) [38] models for nuclear modification of nonresonant inelastic events. Statistical uncertainty and deviations from GENIE are expressed as percentages. The model deviations are calculated using event reweighting, thus there is no statistical variation among models.